Maritime Technology and Research

https://so04.tci-thaijo.org/index.php/MTR

Research Article

Exploring structured scripting cartographic technique of GMT for ocean seafloor modeling: A case of the East Indian Ocean

Polina Lemenkova*

Schmidt Institute of Physics of the Earth of the Russian Academy of Sciences, Department of Natural Disasters, Anthropogenic Hazards and Seismicity of the Earth, Laboratory of Regional Geophysics and Natural Disasters, Moscow, Russia

Article information

Received: December 29, 2020
Revised: January 29, 2021
Accepted: February 1, 2021

Keywords
Ninety East Ridge,
Indian Ocean,
GMT,
Cartography,
Geophysics,
Topography

Abstract

This paper examines spatial variations in the geomorphology of the Ninety East Ridge (NER), located in the Indian Ocean. The NER is an extraordinary long linear bathymetric feature with topography reflecting complex geophysical setting and geologic evolution. The research is based on a compilation of high-resolution bathymetric, geological, and gravity datasets clipped for the study area extent (65° - 107°E, 35°S - 21°N): General Bathymetric Chart of the Oceans (GEBCO), Earth Gravitational Model (EGM2008, EGM96). The submarine geomorphology of the NER was modeled by digitized cross-sectional profiles using Generic Mapping Tools (GMT). The availability of the method is explained by 1) the free datasets; 2) the open source GMT toolset; 3) the available tutorials of the GMT and the codes explained in this work. Three segments of the NER were selected, digitized, and modeled: 1) northern 89°E, 7°S to 90°E, 7°N; 2) central 88.4°E, 14.7°S to 88.8°E, 8.2°S; 3) southern 87.9°E, 17°S to 87.5°E, 27°S. Measured depths were visualized in graphs, compared, and statistically analyzed by the histograms. The northern segment has a steepness of 21.3° at the western slopes, and 14.5° at the eastern slope. The slopes on the eastern flank have dominant SE orientation. The central segment has a bell-shaped form, with the highest steepness comparing to the northern and southern segments. The eastern flank has a steepness of 49.5°. A local depression at a distance of 50 km off from the axis (90°E) continues parallel to the NER, with the shape of the narrow minor trench. The western slope has a steepness of 57.6°, decreasing to 15.6°. The southern segment has a dome-like shape form. Compared to the northern and central segments, it has a less pronounced ridge crest, with a steepness of 24.9° on the west. The eastern flank has a steepness of 36.8° until 70 km, gradually becoming steeper at 44.23°. A local minor trench structure can be seen on its eastern flank (100 km off the axis). This corresponds to the very narrow long topographic depressions stretching parallel to this segment of the NER at 90.5°E. The study contributes to regional geographic studies of Indian Ocean geomorphology and cartographic presentation of GMT functionality for marine research and oceanographic studies.

*Corresponding author: *Schmidt Institute of Physics of the Earth of the Russian Academy of Sciences, Department of Natural Disasters, Anthropogenic Hazards and Seismicity of the Earth, Laboratory of Regional Geophysics and Natural Disasters, Moscow, Russia*
E-mail address: pauline.lemenkova@gmail.com

1. Introduction

The study is focused on the morphological structure of the Ninety East Ridge (further, the NER), located in the eastern part of the Indian Ocean (**Figure 1**). Its name is derived from the specific geographic location and the unique shape form (geometrically elongated and extraordinarily thin, with a width between 150 to 250 km), stretching around the 90°E meridian. With a total length of about 5,000 km, the NER is the longest linear bathymetric feature on Earth and has been studied in various papers (Weis et al., 1991; Silva et al., 2013; Nobre et al., 2013).

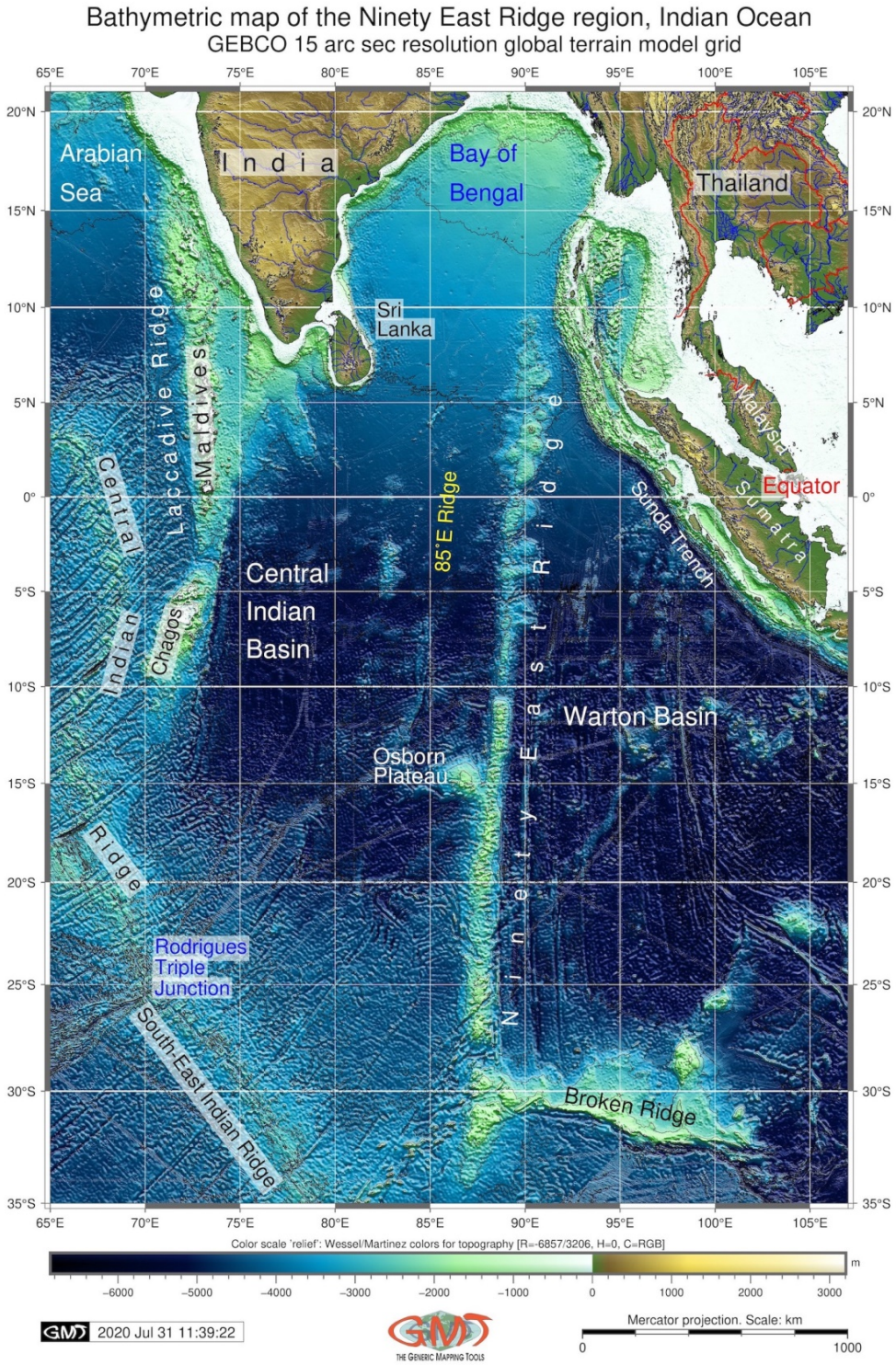

Figure 1 Topographic map of Ninety East Ridge region. Source: author

1.1 Topography and geometric structure

A long and linear aseismic ridge, the NER is the most notable mountainous structure in the eastern part of the Indian Ocean. Its topographic elevations reach ca. 2 - 3 km above the seafloor. The NER marks the principal boundary between the Central Indian Basin and the Wharton Basin, the Indo-Australian intraplate region with repeated earthquakes (Carpenter & Ewing, 1973; Aderhold & Abercrombie, 2016; Stevens et al., 2020). The topography of the NER consists of blocks and mountainous masses (Smith, 1978).

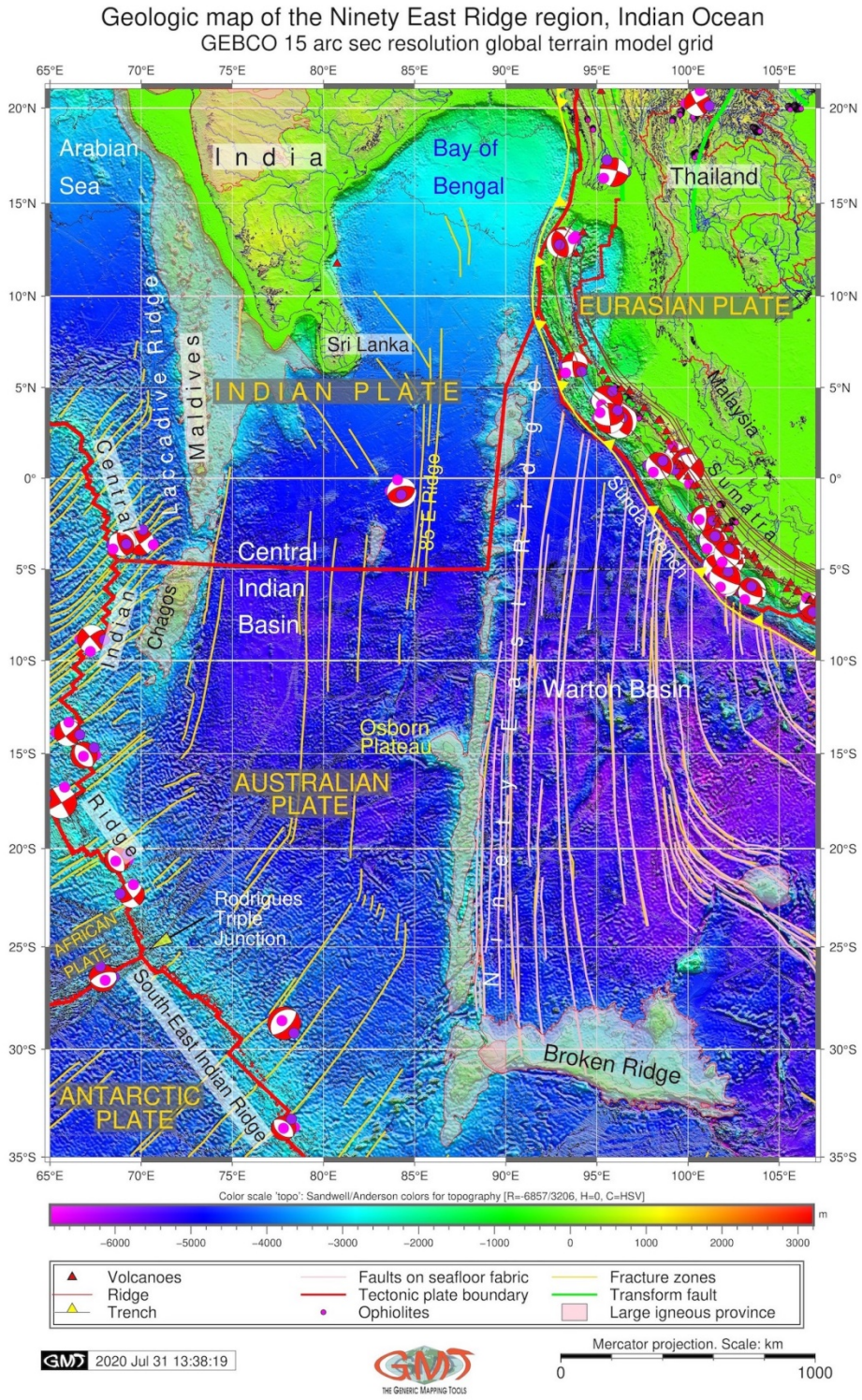

Figure 2 Geologic map of Ninety East Ridge region. Source: author

The total length of the NER is extraordinary among other submarine objects. It stretches at almost 40°: in the south, the ridge starts from the Broken Ridge (ca. 31°S) and continues northwards up to the Bay of Bengal (ca. 9°N). North of the equator, it is subducted below the Andaman Trench (Curray, 2005; Mukhopadhyay & Krishna, 1995). The northward oriented lineaments, genetically related to the NER, continue up to the Shillong Plateau, Indian Shield, in the form of carbonatite intrusives (Gupta & Sen, 1988).

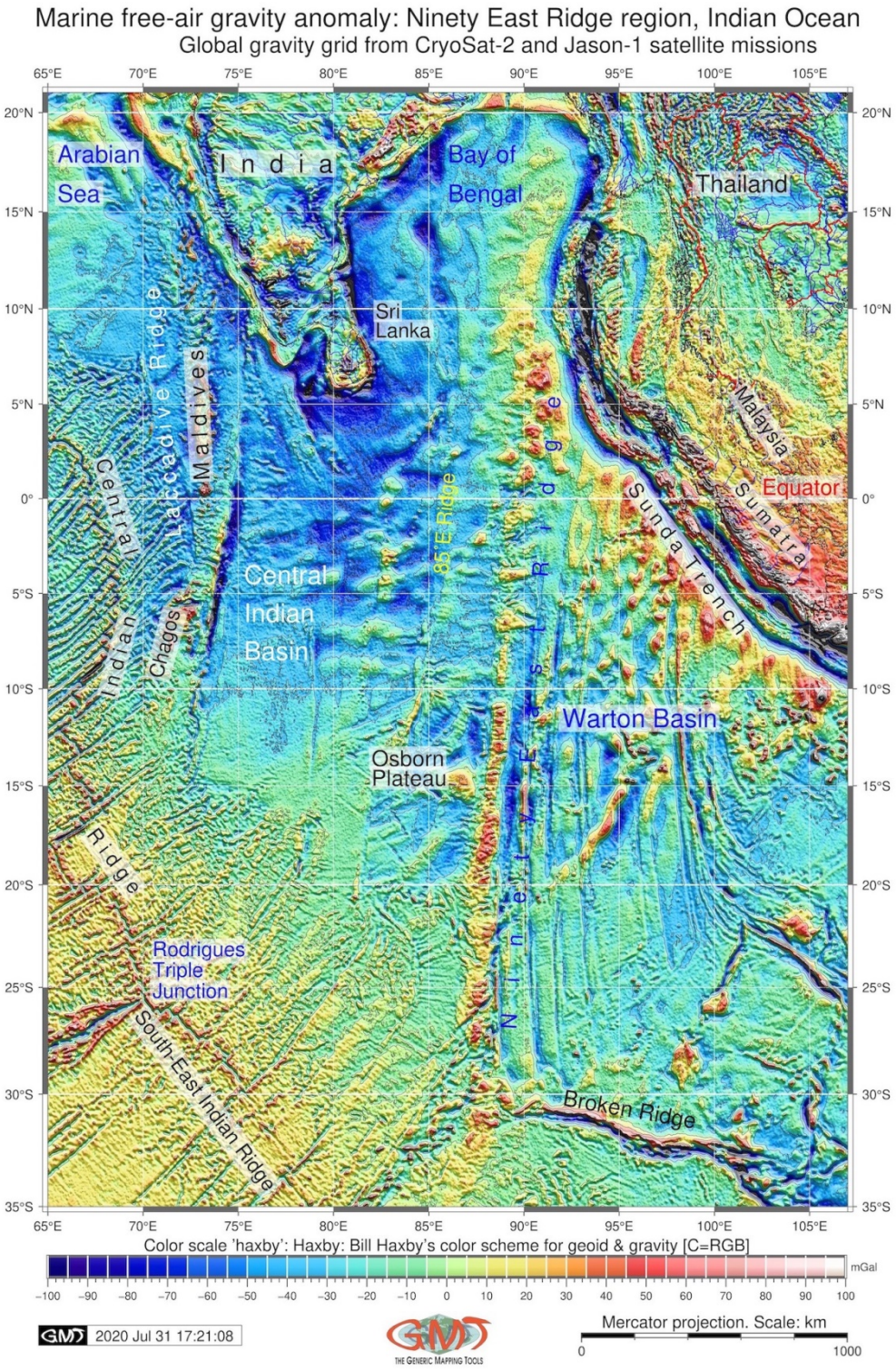

Figure 3 Marine free-air gravity map of Ninety East Ridge region. Source: author

1.2 Geologic setting

The formation of the NER should be introduced in the context of the geologic evolution of the Indian Ocean, since the NER forms an important morphological part of the Indian Ocean. The geologic development of the Indian Ocean, since the Jurassic period, can be generally divided into 3 important periods: 1) from the breakup of Gondwana to the Late Cretaceous- 160 to 90 Ma (opening of the Indian Ocean); 2) the middle Eucene- the collision of India and Eurasia, and 3) the opening of the Gulf of Aden (10 Ma) and the beginning of the intraplate deformation (India-Australia) in the central Indian Ocean (Royer et al., 1992).

Geologically, the NER presents a chain of basaltic submarine volcanoes remaining as a hotspot track from the rapid northward movement of the Indian Plate over the Kerguelen hotspot (Coffin et al., 2002; Frey et al., 2011; Fleet & McKelvey, 1978). Thus, the NER was partly formed as a lithospheric plate boundary between the Indian and Australian tectonic plates during their deformation (**Figure 2**). The seafloor spreading continued until the Eocene epoch of the Paleogene period (ca. 45.6 M).

The Indian, Australian, and Antarctic tectonic plates moved during the Cretaceous and early Cenozoic (Paleogene), about 90 to 45 Ma (Liu et al., 1983). These tectonic processes ultimately initiated the formation of the NER (Kumar et al., 2007; Cande et al., 2010). A fracture zone is generally oriented N–S, parallel to the trend along the eastern margin of the ridge (**Figure 2**). The geological evolution of the NER was affected by active volcanism and sedimentation during the Cretaceous, which was followed by progressive submersion in the Late Cretaceous. As a result, the region has a high level of large earthquakes (Gahalaut et al., 2010). The NER was formed as an emplacement of gabbro and serpentinized peridotite beneath the oceanic crustal layers. Its lithology is mostly composed of basalts derived from the residue of ancient partial melting (Choudhuri et al., 2014; Frey et al., 2015) which point to earlier volcanism. The crustal thickness at the NER is ca. 6.5 - 7 km (Grevemeyer et al., 2001).

Other rock composites include associations of rhyolites and trachytes ,which point to the island-arc nature of the volcanism in the region, as well as the alkaline-ultramafic-carbonatite suite of rocks of seemingly Cretaceous age (Gupta & Sen, 1988), mildly tholeiitic basalts, ferrobasalts, and oceanic andesites (Hekinian, 1974; Smith et al., 1991). The basalts vary in age, with a general increase of age to the north: from ca. 43.2 Ma in the south to 81 Ma in the north (Weis et al., 1993). Basement crystallization ages increase systematically from south to north (Duncan, 1978). Such variations in age may be explained by the northward moving of the plate in the late Mesozoic and Cenozoic. As a result of the tectonic movements, a hotspot in the mantle under the Indo-Australian Plate created the NER. Currently, the average formation rate of the ridge is 9 cm/a.

1.3 Seafloor morphology

Notable geomorphological features around the Ninety East Ridge include the Osborne Plateau and the Eighty Five East Ridge (85°E Ridge). The latter presents a near-parallel ridge extending along 85°E from the Afanasy Nikitin Seamounts northward to the Mahanadi basin (Krishna, 2003; Krishna et al., 2014; Altenbernd et al., 2020; Bastia et al., 2010). It is formed as a result of the sagging of the Earth's crust (Anand et al., 2010). The Osborne Plateau is located at 15°S westward off the NER as a large bathymetric elevation. Fractures in the sedimentary cover of the Osborne Plateau extend to the seafloor surface, indicating high tectonic activity in the past which has continued until the present. These are also presented in the adjacent NER with strong recorded earthquakes (Curray et al., 1982).

Notable undersea morphological objects include the Southeast Indian Ridge, stretching in a NW-SE direction from the Rodrigues Triple Junction (25°S, 70°E), formed as a boundary between the Australian and Antarctic plates during the Oligocene from 33.9 to 23 Ma (Sclater & Fisher, 1974; Small et al., 1999).

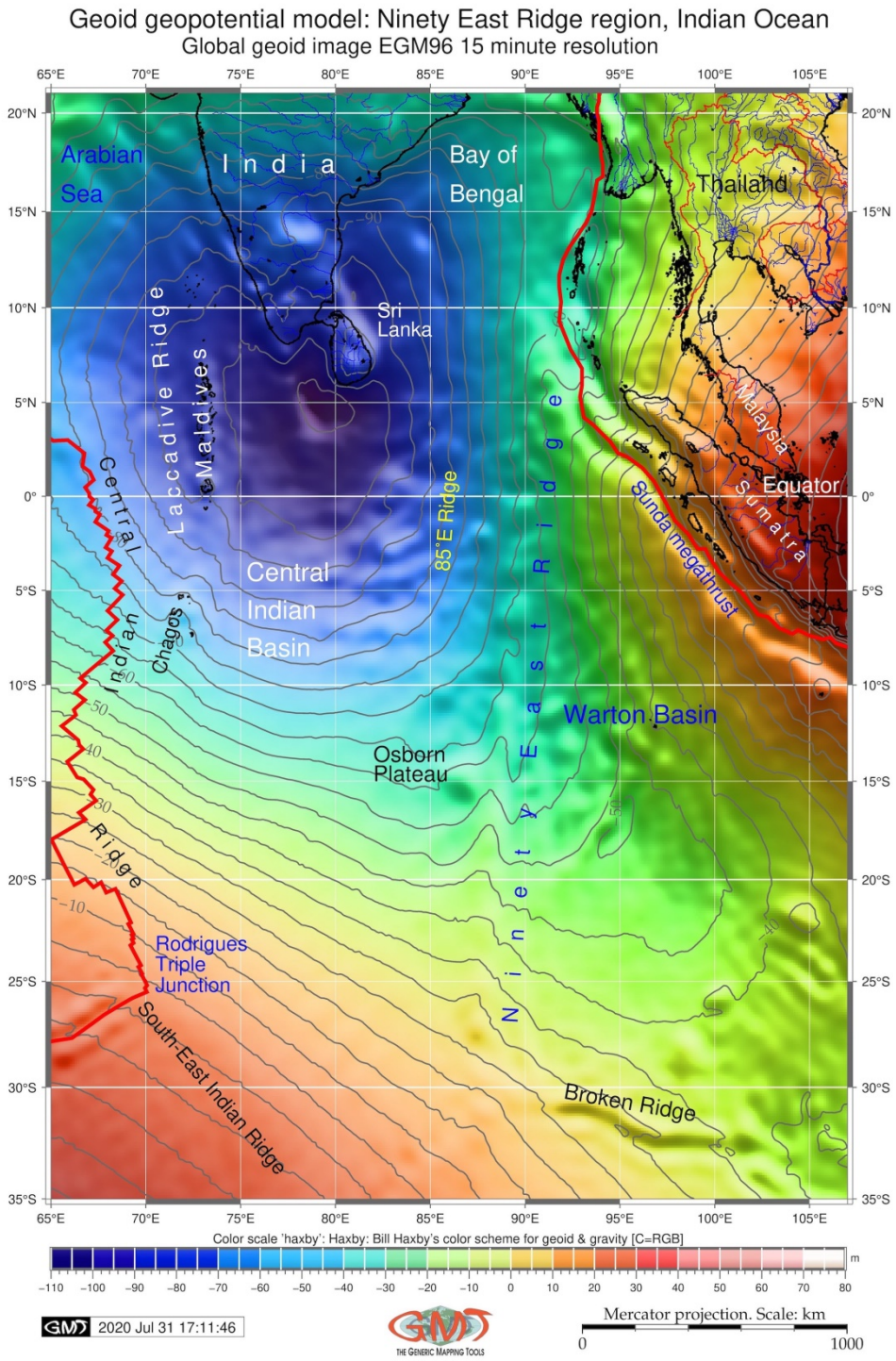

Figure 4 Geoid model of Ninety East Ridge region. Source: author

Another prominent feature in this region that should be mentioned is the Chagos-Laccadive Ridge (CLR), a linear aseismic ridge in the Western Indian Ocean, which is believed to be a trace of the Réunion hotspot (Sreejith et al., 2019).

2. Method and samples

This research employed pre-existing bathymetric (topographic), geophysical and geological datasets available as open source data: General Bathymetric Chart of the Oceans (GEBCO), Earth Gravitational Model (EGM2008, EGM96). Precise bathymetric data provide vital information about undersea areas of the ocean and seafloor relief (Smith, 1993; Smith & Sandwell, 1997; Lemenkova, 2020b, 2020e, 2020f; Marks et al., 2010). Therefore, the General Bathymetric Chart of the Oceans (GEBCO) with SRTM15+ for land areas (Tozer et al., 2019) was selected as a base map for this study (Schenke 2016; GEBCO Compilation Group, 2020). The GEBCO modeling efforts focused on a high-resolution dataset covering the ocean seafloor and terrestrial regions. It employed a 15 arc-second data resolution standard, which resulted in high-precision data (**Figure 1**).

The borders of the plate boundaries, geological lineaments, and vector objects (**Figure 2**) were derived from Bird (2003) and sources of the Scripps Institution of Oceanography (SIO). The research was based on Generic Mapping Tools (GMT) as a main cartographic toolset (Wessel & Smith, 1991; Wessel et al., 2013, 2019). Vector layers (coastal lines, borders, river networks) were applied from the embedded GMT datasets (Wessel & Smith, 1996). The names of the undersea objects were checked using the gazetteer (IHO-IOC GEBCO 2020).

A base map was plotted using the "psbasemap" GMT module, and a visualization of the raster image was performed by the "grdimage" GMT module using the following code: "gmt grdimage ner_relief.nc -Cmyocean.cpt -R65/107/-35/21 -JM6i -P -I+a15+ne0.75 -Xc -K > $ps", as described in a workflow (Lemenkova, 2020a). A more comprehensive interpretation of the quantitative data was carried out by Geospatial Data Abstraction Library (GDAL), a translator library for data formats (GDAL/OGR Contributors, 2020), by the 'gdalinfo' utility: gdalinfo ner_relief.nc -stats, which returned information about the extremal (max/min) data range. Additional elements on maps were added using specific utilities, such as a 'psscale' for adding a color legend and a 'pstext' for adding a text.

The geoid mapping was based on the EGM96 gravity dataset (Lemoine et al., 1998). The research also used the Earth Gravitational Model 2008 (EGM2008) gravity data from the Ninety East Ridge region (Pavlis et al., 2012). The geoid map of the study area is shown in **Figure 4**. The geoid was visualized using a selected example set of commands:

- Making raster image: "gmt grdimage EGM2008ner1.grd -Ccolors.cpt -R65/107/-35/21 -JM6i -P -I+a15+ne0.75 -Xc -K > $ps"
- Adding graticule and title: "gmt psbasemap -R -J -Bpx10f5a5 -Bpyg10f5a5 -Bsxg5 -Bsyg5 -B+t"Geoid geopotential model: Ninety East Ridge region, Indian Ocean" -O -K >> $ps"
- Adding coastlines, borders, rivers: "gmt pscoast -R -J -P -Ia/thinnest,blue -Na -N1/thinner,red -W0.1p -Df -O -K >> $ps"
- Adding texts: "gmt pstext -R -J -N -O -K -F+jTL+f11p,Helvetica,black+jLB+a-53 -Gwhite@40>> $ps << EOF 69.5 -26.4 South-East Indian Ridge EOF"
- Adding legend: "gmt psscale -Dg65/-38+w15.2c/0.4c+h+o0.0/0i+ml -R -J -Ccolors.cpt -Bg5f2a10+l"Color scale 'haxby': Haxby: Bill Haxby's color scheme for geoid & gravity [C=RGB]" -I0.2 -By+lm -O -K >> $ps"
- Converting to image file by GhostScript: "gmt psconvert Geoid_NER.ps -A1.0c -E720 -Tj -Z"

Cartographic visualization of the Earth's gravity fields from various datasets has been presented in the existing literature (Andersen & Knudsen, 1998; Barzaghi et al., 2015; Sansò et al., 2019; Lemenkova, 2019d, 2019e; Balmino; 2003). The applied gravity dataset in this study (**Figure 3**) is the result of the global marine gravity modeling from CryoSat-2 and Jason-1 (Sandwell et al., 2013; Sandwell et al., 2014). The collection of such multi-disciplinary data is an important task for geophysical studies of the Ninety East Ridge. Data processing, technical details of GMT modules,

and scripting approaches applied to these data are explicitly described in the existing works (Wessel et al., 2013; Wessel & Smith, 1998; Lemenkova, 2019a; Lemenkova, 2019b; Lemenkova, 2019c).

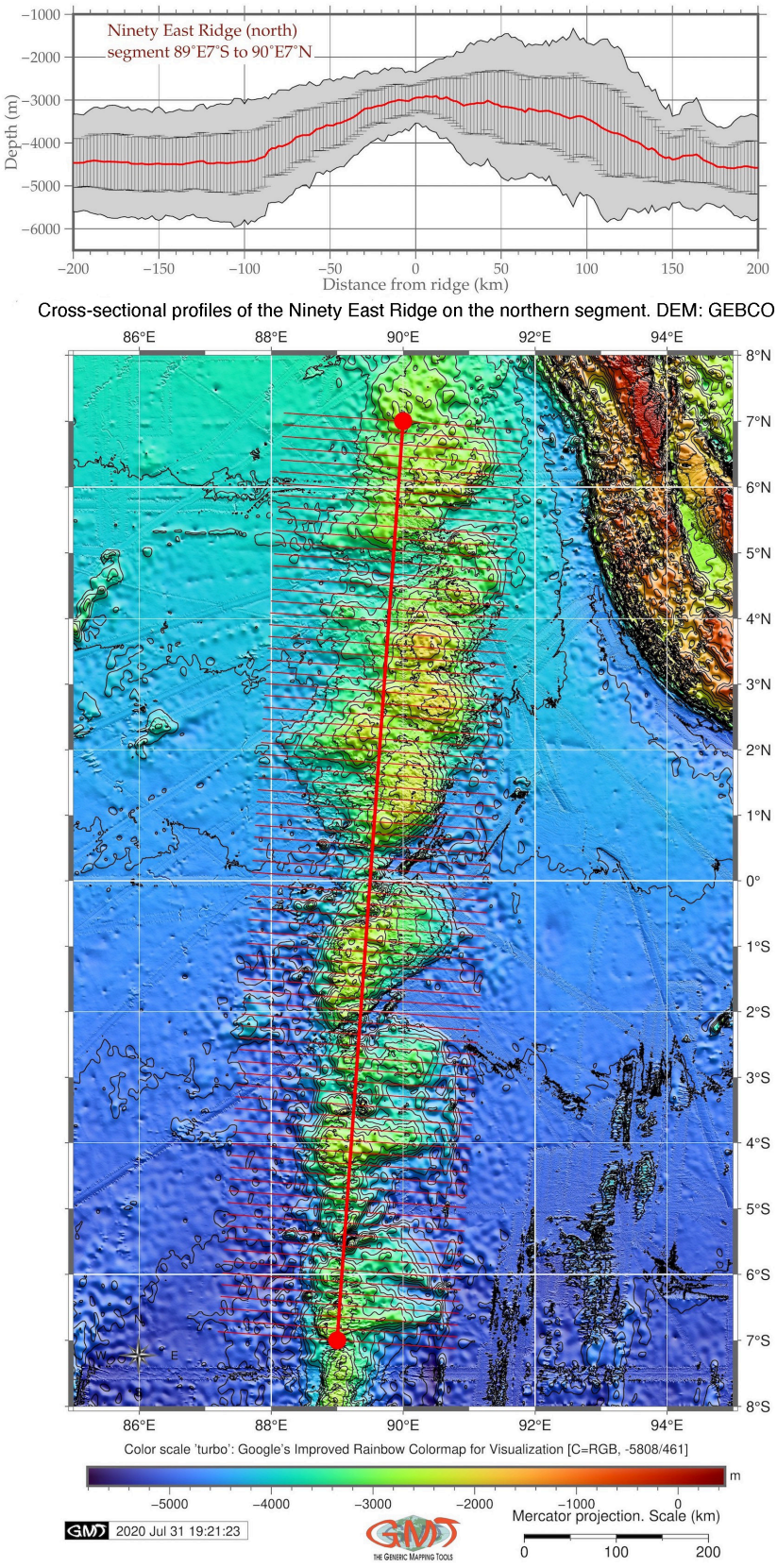

Figure 5 Cross-section profiles of Ninety East Ridge: north. Source: author.

Color palettes for the gravity and geoid maps were applied from the GMT embedded data. The extracting of the file subset in an IMG format and the converting of it to a GRD format was done using the 'img2grd' GMT module using the following code: 'img2grd grav_27.1.img -R65/107/-35/21 -GgravNER.grd -T1 -I1 -E -S0.1 -V'. Here, the module read an IMG format file, extracted a subset with the coordinates 65/107/-35/21, and wrote it to a grid file 'gravNER.grd'. Following this, the image was visualized using the 'grdimage' GMT module by applying Haxby color palette. The gravity contours of 30 mGal were drawn using the gridded dataset of gravity.

Three cross-sectional segments across the NER were digitized (**Figures 5 - 7**) in the 3 segments of the NER, to generate the integrated topographic-morphological models of its submarine relief. This approach employed an automated GMT-based modeling technique to generate a set of perpendicular cross-sectional models along the 3 selected segments of the NER. The coordinates of the segments were as follows (always from the southern point to the northern): 1) segment 89°E, 7°S to 90°E, 7°N; 2) segment 88.4°E, 14.7°S to 88.8°E, 8.2°S, and 3) segment 87.9°E, 17°S to 87.5°E, 27°S. Thin parallel lines presented the profiles used for automatic digitizing as bathymetric modeling (red-colored on **Figures 5** and **7** and white-colored on **Figure 6**). Thick points with corresponding colors outlined the start and end points for each of the segments. The modeling was done using a selected example set of commands:

- Selecting 2 points along the NER: "cat << EOF > NER1.txt 90.0 7.0 89.0 -7.0 EOF"
- Plotting ridge segment and end points "gmt psxy -Rner_relief1.nc -J -W2p,red NER1.txt -O -K >> $ps # line gmt psxy -R -J -Sc0.15i -Gred NER1.txt -O -K >> $ps # points"
- Generating cross-track profiles 400 km long, spaced 20 km, sampled every 2km and stack these using the mean, write stacked profile: "gmt grdtrack NER1.txt -Gner_relief1.nc -C400k/2k/20k+v -Sm+sstackNER1.txt > tableNER1.txt gmt psxy -R -J -W0.5p,red tableNER1.txt -O -K >> $ps"

Examples of the digitizing using traditional GIS, such as ArcGIS, exist, integrating digital datasets into an accessible framework for comprehensible mapping (Howland et al., 2020; Deng et al., 2013). However, compared to the traditional GIS, the advanced GMT-based cartographic approach includes a higher functionality, such as dynamic scripting, applied mapping design, geovisualization technological re-usability of scripting, and applications for other study areas which facilitate cartographic interaction, and improves mapping workflow. The modeled morphological structure is based on the GEBCO bathymetric data. To create a set of the cross-sectional profiles shown in **Figures 5 - 7**, the topographic GEBCO data were gridded at 10 km spacing and sampled every 2 km with a line of 400 km long for each transect. The elevation values employed were based on the conversion of the machine-based measurements of the observed depths along each cross-section in the region, using the table automatically generated through scripting using the following code: "gmt grdtrack NER1.txt -Gner_relief1.nc -C400k/2k/20k+v -Sm+sstackNER1.txt > tableNER1.txt".

The table 'tableNER1.txt' then contained XY coordinates and a Z-value (depth). The table was then visualized on the upper plot above each of the graphs (**Figures 5 - 7**). The red line on the upper graph (**Figures 5 - 7**) is based on the average median distance between the bathymetric data points and stacked with error bars (thin grey lines in **Figures 5 - 7**) for the upward continuation, reduction to pole, and band pass filters to the grids. The upper and lower values were encountered as an envelope using codes: "gmt convert stackNER1.txt -o0,5 > envNER1.txt" and "gmt convert stackNER1.txt -o0,6 -I T >> envNER1.txt".

The perpendicular cross-sectional profiles were plotted using the following code: "gmt psxy -R -J -W0.5p,red tableNER1.txt -O -K >> $ps". The red line on the plots helped separate all measured cross-sectional data from the statistical median and highlight the data that played an important role in the final interpretation. The GMT module 'grdconcour' was also applied in gravity

mapping for plotting isolines every 30 mGal using the GMT code: "gmt grdcontour gravNER.grd -R -J -C30 -W0.1p -O -K >> $ps". The coastlines, borders, and rivers were added on the maps using GMT module 'pscoast', filtering river networks and borders related to major geographical objects and map elements: "gmt pscoast -R -J -P -Ia/thinnest,blue -Na -N1/thinner,red -W0.1p -Df -O -K >> $ps".

3. Results and discussion

Although technical integration of the raster datasets using GMT scripting techniques lead to important insights into the morphology of the Ninety East Ridge, it is the geological interpretation of the resulting maps that was the main strength of the research methodology. The collected and visualized geophysical, topographic, and geological data were, thus, also integrated to gain synthesis and added knowledge beyond the existing descriptions of the study area (Souriau, 1981; Grevemeyer & Flueh, 2000; Petroy & Wiens, 1989).

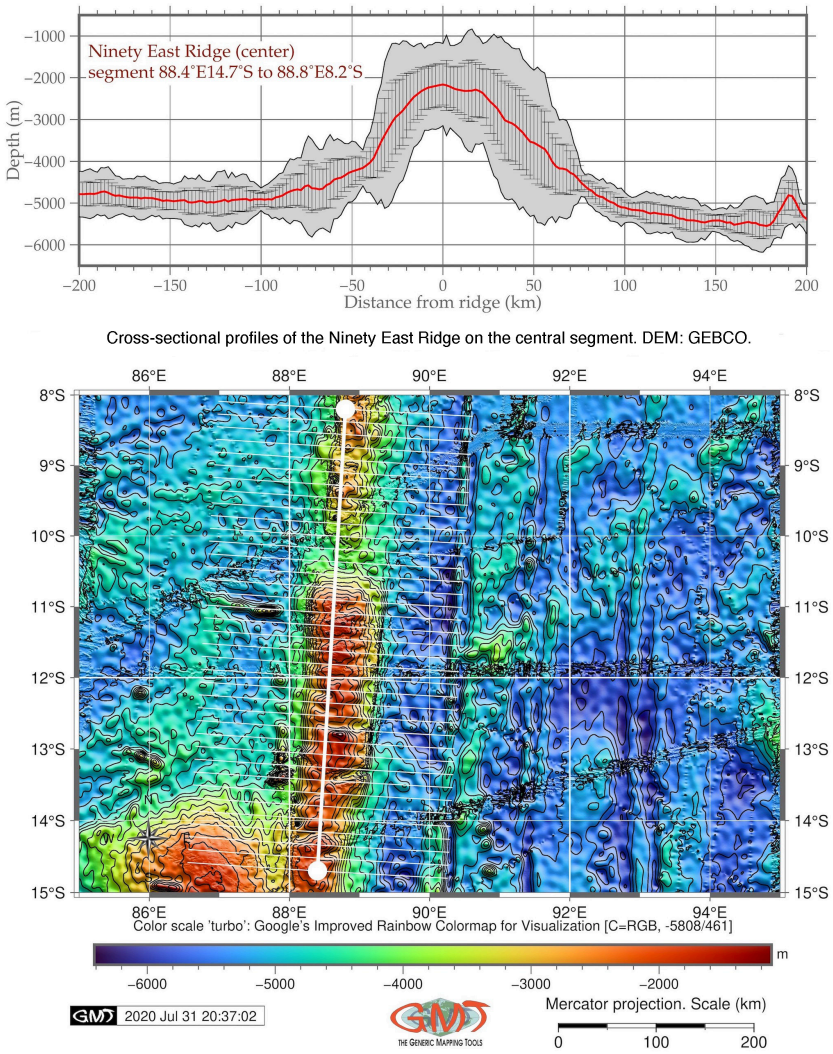

Figure 6 Cross-section profiles of Ninety East Ridge: Central. Source: author

For example, based on the existing papers on the predicting gravity observations from the bathymetry, the topography results from variations of the Earth's lithosphere thickness and mantle density variations (Steinberger, 2016; McKenzie & Bowin, 1976). Thus, information can be obtained by the comparative modeling of the gravity (**Figure 3**) and bathymetry (**Figure 1**).

Satellite-derived data (**Figure 3**) show the marine free-air gravity anomaly associated with the area surrounding the NER. The observed anomaly highs correspond to vertical geological lineaments of the fracture zones or fault structures that can be seen in **Figure 2** (yellow thick lines).

The NER stands out clearly in the gravity field. It is characterized by positive free-air anomalies, with a maximum of up to +60 mGal, and a distinct correlation with the undersea bathymetry, which corresponds with the earlier published studies (Rajesh & Majumdar, 2009). There is also a linear gravity anomaly mirroring the topographic isolines parallel to the NER. If comparing topographic segments of the ridge, the crest areas (the highest elevations) can be seen at values of 50 - 60 mGal (bright red colored areas in **Figure 3**). Deep areas and depressions (Central Indian Basin, the area southward of Sri Lanka, areas of the deep-sea Sunda Trench) correspond to the lowest values below −65 mGal (dark blue colors in **Figure 3**). The South East Indian Ridge has dominating values of 10 - 20 mGal (light yellow colors, **Figure 3**). In the Bay of Bengal, the marine gravity field gradually decreases to slightly negative values (0 to −10 mGal), where overlying sediments have smaller density contrasts compared to the ridge basalts. The existing maps (Royer et al., 1989) present Geosat mapping of the topography of the equipotential sea surface, or marine geoid, in the Indian Ocean. The presented maps (**Figures 3** and **4**) show the updated visualization using the modern available datasets of EGM-2008 and gravity grids. Geological lineaments, such as fracture zones in the Wharton Basin, South East Indian Ridge, and Central Indian Basin (**Figure 2**), also correlate with gravity isolines (**Figure 3**). Existing studies report gravity and bathymetric variations in selected northern, central, and southern segments of the NER. Tiwari et al., (2003) suggested that northern and southern parts of the NER with compensated elastic thickness were emplaced off to a ridge axis.

On the contrary, the central segment (near the Osborn Plateau) has a locally compensated large topography and a thick crust which could be moved near a spreading center. Such a complex process could result from the interaction of a hot spot with the spreading ridge in the NER area. Large igneous provinces (LIPs) which include iron- and magnesium-rich rocks (pink-colored areas in **Figure 2**) show large accumulations of igneous rocks, both intrusive and extrusive (from lava flows), resulting from magma eruption through the Earth's crust towards the seafloor surface. Besides the NER, LIPs can be also seen on the Broken Ridge, the Chagos-Lakkadive Ridge, and the Maldives. Generally, LIPs are proof of tectonic activities in the past (Neal et al., 2015).

Along its length, the ridge is divided into 3 distinct morphological segments. The comparison of these transects (**Figures 5 - 7**) shows that the ridge is not continuous, and occurs as varied linear structural highs with interspersed local depressions and rifts that have different morphological and topographical structures:

1. The northern segment (**Figure 5**) has a median steepness of 21.3° at the western slopes and 14.5° at the eastern slope. The slopes on the eastern flank have dominant SE orientation. The distribution of data on the minimal depths has a pyramid-shaped peak with steep walls. The adjusting seafloor topography eastward of the northern segment has an almost flat relief (dark blue areas in **Figure 5**) contrasting with the ridge. The western region also has less pronounced variations compared to other segments.

2. The central segment (**Figure 6**) has an almost classic bell-shaped form, with the highest steepness compared to the northern and southern segments. A local depression can be seen at a segment of 10.0° - 10.6° S of the ridge, separating it into the 2 uneven parts. The eastern flank has a steepness of 49.5° and gradually continues eastward. A local depression at a distance of 50 km from the axis (at almost 90°E) continues parallel to the NER with a shape of the narrow minor trench. The western slope has a steepness of 57.6° until 40 km from the axis; afterwards, the steepness decreases to 15.6° and the relief becomes gentle. Narrow long topographic depression strikes running parallel to the ridge in the eastern part of the seafloor off the ridge axis are notable in the central segment.

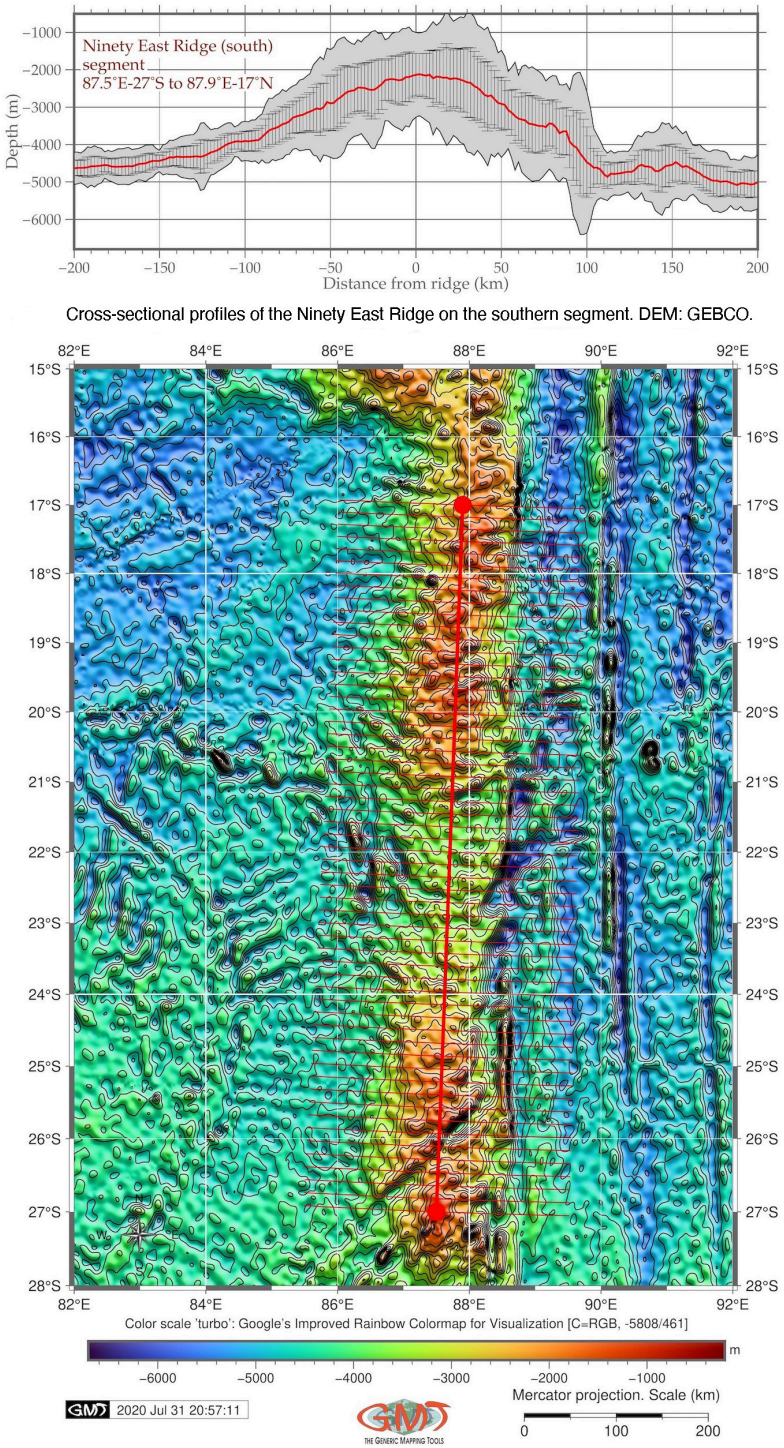

Cross-sectional profiles of the Ninety East Ridge on the southern segment. DEM: GEBCO.

Figure 7 Cross-section profiles of Ninety East Ridge: South. Source: author

3. The southern segment (**Figure 7**) has a dome-like shape form and several subtle offshoots parallel to the main ridge axis on its eastern flank. Compared to the northern and central segments, it has a less pronounced crest of the ridge, with a steepness of 24.9° on its western flank. On the contrary, its eastern flank has a steepness of 36.8° until 70 km, and then becomes steeper at 44.23°. Local minor trench structure can be seen on its eastern flank at 100 km off the axis. This corresponds to a very narrow long topographic depression stretching parallel to this segment of the NER at 90.5°E (**Figure 7**). The southern segment also shows a steep downward topographic depression between 89°E and 91°E, as clearly seen in **Figure 7** (dark blue colors, narrow strip lines

indicating local minor trench). Such faults, located parallel to the NER, extend in the southern segment (15° - 25°S). Their origin could be caused by changes in the direction of the spreading ridge between 86° - 90°E.

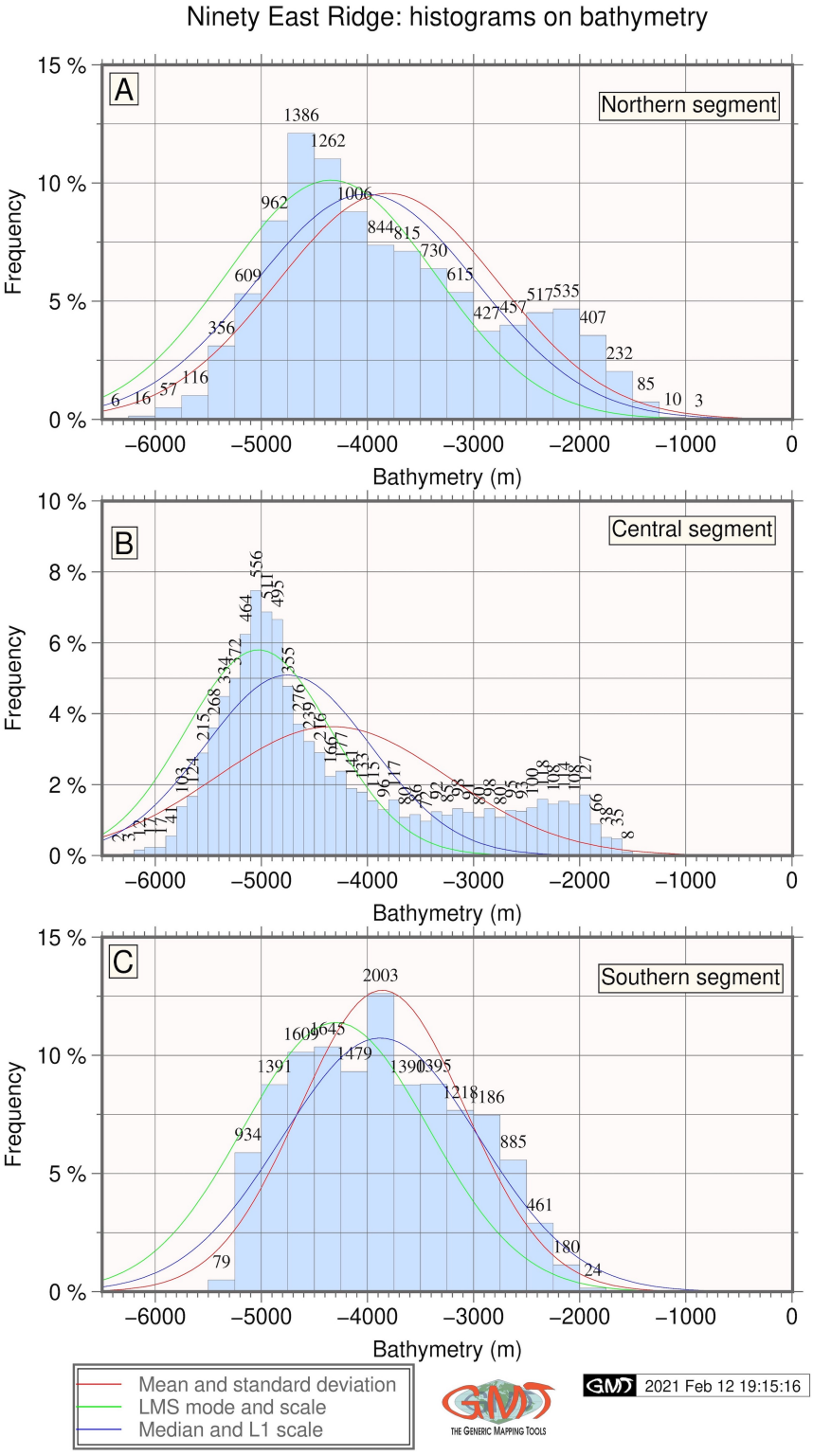

Figure 8 Statistical histograms of cross-sections of Ninety East Ridge. Source: author

The crest of the NER in the northern segment (7°N to 7°S) is generally deeper (as shown in the graph of **Figure 5**), with median depth not exceeding −3,000 m. On the contrary, the southern segment has median values of the crest up to −2,400 m (**Figure 6**) and also (**Figure 7**) shows the highest crest elevation up to −2,200 m of the median (red line on the graph). The SW-NE directed deep-seated fractures can be also seen in the southern segment between 25.2°S to 27.0°S.

The descriptive statistical analysis of the 3 segments of the ridge (**Figure 8**) shows certain differences in the depth distribution in the northern, central, and southern parts of the NER, which supports previous remarks. The most repetitive depths for the southern segment "A", central segment "B", and northern segment "C" are visualized. Of these graphs, the southern segment (**Figure 8C**) has the most bell-shaped data distribution character, which means the clearly shaped form of the ridge sharply contrasts with the surrounding relief. The majority of data are concentrated within the range of −5,000 to 2,250 m. Other values are insignificant and do not exceed 80 sample points. The most often seen repetitive values are detected at the range of depths −3,750 m to −4,000 m (2,003 samples), **Figure 8C**.

The central segment of the NER, displayed in graph "B" (**Figure 8B**), shows a wedge-like data distribution for the range −6,000 to −3,600 m. Maximal values are detected at −5,000 to −5,100 (556 samples). Higher elevations (from −3,600 to −2,000 m) show an almost uniform data distribution at about 90 samples in each bin. Statistically, these values do not exceed 2 %. The northern segment (**Figure 8A**) shows a 2-peak data distribution with clearer and more distinct peaks at depths range between −4,000 to −5,000 m: above 7,5 % of all values, above 900 samples in each bin. The most frequent values are 1,386 observation samples at depths between −4,500 to −4,750 m. The values then gradually decrease until −3,000 m, when the depths increase a little again with values in the interval of −3,000 to −2,000 m, though in generally do not exceed 5 % of the whole range. Comparing all the 3 segments, most of the data pool is located in the range of −6,000 to −3,000 m, with the central segment as the deepest, with only a few data samples exceeding −6,000 (17 samples in the central segment, and 22 samples in the northern segment).

4. Conclusions

Results presented in this paper include comparison of the 3 segments of the NER regarding the geophysical and geologic settings in the respective areas, using the 3 color representation schemes matched with the 'turbo' Google's improved color representation schemes for visualizing depths variations. The presented results are organized by cartographic visualization, using larger scales for the visualizing of the 3 NER segments and smaller scales for the regional mapping of the NE Indian Ocean. In addition, the results for the bathymetric mapping are compared with those of the geoid and geophysical gravity fields modeled using the GMT-based module mapping, in which high-resolution raster grids (EGM-2008 and gravity grids) are used to depict variations in the values (mGal for the free-air gravity and m for the geoid) to represent the relationship of geophysical setting with topography. The relationship between geoid height and topography was discussed and well-explained by Sandwell and McKenzie (1989). In brief, the topography of the oceanic plateaus and swells is affected by crustal thickening, thermal buoyancy forces in the lithosphere, and local compensation from flexural and deep mantle signals.

Another parameter affecting the gravity field and topography is sedimentation. The effects of sedimentation on continental gravity field and topography were demonstrated in previous studies (Sandwell & Liu, 1985; Lemenkova, 2020c), showing the topography smoothed by sediments of the Bengal Fan in the northern Indian Ocean. However, the correlation of seafloor topography with kinetic energy differs with depth, being greater over smooth abyssal plains than over rough bathymetry, and vice versa, since bottom roughness may dissipate eddy kinetic energy at higher depths (Gille et al., 2000). The comparison of the topography of the NER with geophysical and regional geologic settings in the north-east Indian Ocean makes it possible to assess the relative

effectiveness of the geophysical parameters as the impact for the formation of topographic structures. Using high-resolution datasets, such as GEBCO, EGM-2008, and gravity grids by Sandwell et al. (2014), adds reliability and precision to the final outputs and presented maps.

In the course of its geologic evolution, the NER has been affected by a variety of geological processes: northward motion of the Indian Plate (Peirce, 1978), subsidence, movements between spreading centers, and the Earth's mantle structure deformation of crustal blocks (Krishna et al., 2001; Rao et al., 1997). Impact factors that could have an effect on the deepening of the NER topography in the central segment include plate motions, hot spot activity, topographic closeness of the hot spots to the NER, and tectonic factors such as an intra-plate compression strength. As a result of these factors and complex interactions between the geologic processes, the seafloor bathymetry of NER is highly undulated and asymmetric in various segments. The morphology includes steep rises and slopes, and an uneven distribution of depths and slope gradients, as demonstrated in this work, based on the GEBCO dataset modeling. The topography also has a notable correlation with the distribution of the gravity anomaly fields.

Spatial distribution of the morphological structures and topography present in the NER reflects its geological evolution and tectonic history. Both plate movements and varying spreading ridge rates contributed to the ultimate formation of the contemporary bathymetry of the NER. The sediment accumulation, to a certain extent, has also exerted an influence on the crest form and ridge morphology. Supported by the geophysical and geologic mapping based on the high-resolution grids, this study highlights spatial differences as a comparative submarine morphology and bathymetry of the ridge structure in its northern, central, and southern segments. It also presents a comparison between the several geophysical datasets, high-resolution bathymetry, and geologic data. The cross-section profiles presented in this paper and supplemented by the visualized geophysical grids of geoid and gravity anomalies clearly bring out the undersea morphology of the NER in the 3 segments: 1) northern segment 89°E, 7°S to 90°E, 7°N; 2) central segment 88.4°E, 14.7°S to 88.8°E, 8.2°S, and the 3) southern segment 87.9°E, 17°S to 87.5°E, 27°S.

The distinct presence of upward dome-shape, wedge-shape and bell-shape morphological configurations within the 3 segments mapped on the ridge (**Figures 5 - 7**) supports its volcanic origin with multiple volcanic episodes. These specific geomorphological structure characteristics suggests the conclusion that the formation of the NER was connected with the tectonic movement of the Indian Plate over the Kerguelen hotspot, which produced the basaltic lava forming the ridge. However, Flee and McKelvey (1978) indicated earlier that NER volcanism was different from that which produces mid-ocean ridge basalts; the sequence of basaltic rocks from the NER is enriched by heavy rare earth elements, although their contents vary unsystematically with depth. Thus, basement lavas from certain sites in the NER are tholeiitic basalts, while lavas appear to be subaerial eruptives, but the lowermost flows are pillow lavas (Frey et al., 1991). This phenomena might be caused by high-temperature subaqueous alteration and the presence of biogenous calcite.

Various publications have discussed the origin and specifics of the NER morphology, including the theory of the mode of emplacement using interpretation of the available geophysical data, including aspects of hot-spot formation, active faulting, and deformation of the Indian Plate (Subrahmanyam et al., 2008; Sager et al., 2013; Ratheesh et al., 2013; Hédervari, 1982; Royer & Sandwell, 1989). For instance, the time and mode of NER emplacement during the evolution of the Indian Ocean includes its long trace from the Afanasy Nikitin Seamount and many complex movements that finally caused asymmetries in its morphology. This study, supported by previous tectonic modeling (Royer et al., 1991), indicates that the NER originated from a hot spot in the Indian Ocean. This caused plate movements varying in rate and intensity in its different age and locations. Finally, this resulted in its present asymmetric morphology. Bathymetry and gravity data in the southern segment of the NER to the east revealed steep downward faulting of approximately 2 km. This local narrow depression is presented by the fracture zones with undulated topography (minor trench stretching parallel to the NER).

Theoretical and quantitative progress in computer technologies have brought dramatic changes in the methodology of modeling and cartographic mapping in geological and geographical studies, rapidly and continuously developing since the 1960s (Stocks, 1960; Chang, 1982; Liu et al., 1982; Suetova et al., 2005a; Suetova et al., 2005b; Gohl et al., 2006a; Gohl et al., 2006b; Schenke & Lemenkova, 2008; Lemenkova, 2020d; Shang et al., 2020). As demonstrated in this paper, using multi-source geophysical, geological, and topographic data with high-resolution facilitates comparison of the geological phenomena and the finding of correlations between the morphology of the NER and local geophysical settings.

The GMT scripting approach, in contrast to the traditional GIS, enables the creation of an elaborated model of topographic cross-sectioning using quantitative variables as depths. Depending on the local geophysical context, such models can express spatial distributions of the depths, trends in slope steepness, and sectors of the extended anomalous depths (southern, central and northern), pointing at minor trenches parallel to ridges. Traditional GIS approaches are popular and widely used (e.g., Klaučo et al., 2013; Klaučo et al., 2014; Klaučo et al., 2017). However, the standard GIS often requires the generation of a GIS project and a handmade routine, while GMT applies scripting algorithms similar to programming languages in its paradigm, such as Python, AWK, or R (e.g., Lemenkova, 2019f; Lemenkova, 2019g; Lemenkova, 2019h). Using scripting syntax in cartographic mapping enables the modification of maps on the fly, using existing templates or performing statistical analysis (e.g., Lemenkova, 2018). This significantly facilitates the process and increases both the precision and the design quality of the output maps. An alternative way of bathymetric mapping is a combination of various methods by using both scripts and a traditional GIS (Gauger et al., 2007).

Due to its complex geologic evolution, the morphology of the NER differs in the 3 diverse segments, which is caused by the Indian Plate movements and the hot spot volcanism near the Kerguelen Plateau. Besides the morphological analysis of the NER, the technical purpose of this work was to give a tangible demonstration of the usefulness of representing high-resolution geophysical and topographic raster grids for analysis of seafloor morphology at regional and local extends using advanced cartographic solutions and modeling methods of GMT. With this aim in mind, 3 automatically-digitized segments of the NER were prepared and visualized, showing how the ridge generally differs in a profile view over its extend, what its slope gradient are, and what depth frequencies are in the 3 segments.

The paper contributed to the 3 research aspects:

1) geological studies of the NER as a unique geological submarine object,
2) cartographic demonstration of geophysical and bathymetric mapping by GMT,
3) technical questions of the data visualization in geology.

All illustrations were plotted in GMT using regional and local scales: regional scale refers to **Figures 1 - 4** and local enlarged scales represent 3 segments of the NER (**Figures 5 - 7**). A statistical graph shows the comparison of bathymetry (**Figure 8**). Brief explanations of the GMT modules and their technical workflow are provided. The actuality of using GMT for the marine geological studies is caused by the specifics of the study object: modeling seafloor morphology requires indirect (R/V-based) observations, extensive analysis of the existing geological literature, and visualization of the geophysical and bathymetric datasets. In view of this, data visualization and computer-based methods in geological mapping of the seafloor and modeling its relief are progressive and advanced methods, as demonstrated in this article.

Acknowledgments

I thank the 3 anonymous reviewers and the editor for their comments and suggestions which improved the initial manuscript. The research was implemented into the framework of the project No. 0144-2019-0011, Schmidt Institute of Physics of the Earth, Russian Academy of Sciences. I

thank the GMT developers, P. Wessel and W.H.T. Smith, for the creation of this cartographic toolset. Compared to all other GIS and mapping software, it is simply the best.

References

Aderhold, K., & Abercrombie, R. E. (2016). Seismotectonics of a diffuse plate boundary: Observations off the Sumatra-Andaman trench. *Journal of Geophysical Research: Solid Earth, 121*, 3462-3478. doi:10.1002/2015JB012721

Altenbernd, T., Jokat, W., & Geissler, W. (2020). The bent prolongation of the 85°E Ridge south of 5°N - Fact or fiction? *Tectonophysics, 785*, 228457. doi:10.1016/j.tecto.2020.228457

Anand, S. P., Rajaram, M., Majumdar, T. J., & Bhattacharyya, R. (2009). Structure and tectonics of 85°E Ridge from analysis of Geopotential data. *Tectonophysics, 478*(1-2), 100-110. doi:10.1016/j.tecto.2008.09.036

Andersen, O., & Knudsen, P. (1998). Global marine gravity field from the ERS-1 and GEOSAT geodetic mission altimetry. *Journal of Geophysical Research, 103*, 8129-8137. doi:10.1029/EO068i002p00017

Barzaghi, R., Migliaccio, F., Reguzzoni, M., & Albertella, A. (2015). The Earth gravity field in the time of satellites. *Rendiconti Lincei. Scienze Fisiche e Naturali, 26*, 13-23. doi:10.1007/s12210-015-0382-9

Balmino, G., Moynot, B., Sarrailh, M., & Valès, N. (1987). Free air gravity anomalies over the oceans from Seasat and Geos 3 altimeter data. *Eos, Transactions American Geophysical Union 68*(2), 17-19. doi:10.1029/EO068i002p00017

Balmino, G. (2003). *Gravity Field Recovery from GRACE: Unique Aspects of the High Precision Inter-Satellite Data and Analysis Methods*. In Beutler, G., Drinkwater, M. R., Rummel R., Von Steiger, R. (Eds). Earth Gravity Field from Space: From Sensors to Earth Sciences. Space Sciences Series of ISSI, 17. Springer, Dordrecht. doi:10.1007/978-94-017-1333-7_5

Bastia, R., Radhakrishna, M., Das, S., Kale, A. S., & Catuneanu, O. (2010). Delineation of the 85°E ridge and its structure in the Mahanadi Offshore Basin, Eastern Continental Margin of India (ECMI), from seismic reflection imaging. *Marine and Petroleum Geology, 27*(9), 1841-1848.

Bird, P. (2003). An updated digital model of plate boundaries. *Geochemistry, Geophysics, Geosystems, 4*(3), 1027. doi:10.1029/2001GC000252

Bowin, C. (1973). Origin of the Ninetyeast Ridge from studies near the equator. *Journal of Geophysical Research, 78*, 6029-6043. doi:10.1029/JB078i026p06029

Cande, S. C., Patriat, P., & Dyment, J. (2010). Motion between the Indian, Antarctic and African plates in the early Cenozoic. *Geophysical Journal International, 183*(1), 127-149. doi:10.1111/j.1365-246X.2010.04737.x

Carpenter, G., & Ewing, J. (1973). Crustal deformation in the Wharton Basin. *Journal of Geophysical Research, 78*(5), 846-850. doi:10.1029/JB078i005p00846

Chang, K. T. (1982). Multi-component quantitative mapping. *The Cartographic Journal 19*(2), 95-103. doi:10.1179/caj.1982.19.2.95

Choudhuri, M., Nemèok, M., Stuart, C., Welker, C., Sinha, S. T., & Bird, D. (2014). 85°E Ridge, India: Constraints on its development and architecture. *Journal of the Geological Society of India, 84*, 513-530. doi:10.1007/s12594-014-0160-9

Cochran, J. R., & Sempéré, J. C. (1997). The Southeast Indian Ridge between 88 E and 118 E: Gravity anomalies and crustal accretion at intermediate spreading rates. *Journal of Geophysical Research: Solid Earth, 102*(B7), 15463-15487. doi:10.1029/97JB00511

Coffin, M. F., Pringle, M. S., Duncan, R. A., Gladczenko, T. P., Storey, M., Müller, R. D., & Gahagan, L. A. (2002). Kerguelen Hotspot Magma output since 130 Ma. *Journal of Petrology, 43*(7) 1121-1137. doi:10.1093/petrology/43.7.1121

Curray, J. R., Emmel, F. J., Moore, D. G. & Raitt, R. W. (1982). *Structure, Tectonics, and Geological History of the Northeastern Indian Ocean*. In Nairn, A. E. M., & Stehli, F. G. (Eds). The Ocean Basins and Margins. Springer, Boston. doi:10.1007/978-1-4615-8038-6_9

Curray, J. R. (2005). Tectonics and history of the Andaman Sea region. *Journal of Asian Earth Sciences, 25*, 187-232. doi:10.1016/j.jseaes.2004.09.001

Deng, M., Liu, G., & Hu, Y. (2013). *Materialization of a comprehensive digital city with CityMaker and ArcGIS*. In Proceedings of the IEEE International Conference on Green Computing and Communications and IEEE Internet of Things and IEEE Cyber, Physical and Social Computing (pp. 1424-1428). Beijing. doi:10.1109/GreenCom-iThings-CPSCom.2013.249

Duncan, R. A. (1978). Geochronology of basalts from the Ninetyeast ridge and continental dispersion in the eastern Indian Ocean. *Journal of Volcanology and Geothermal Research, 4*(3-4), 283-305. doi:10.1016/0377-0273(78)90018-5

Fleet, A. J., & McKelvey, B. C. (1978). Eocene explosive submarine volcanism, Ninetyeast Ridge, Indian Ocean. *Elsevier Oceanography Series, 21*, 73-97. doi:10.1016/0025-3227(78)90047-6

Frey, F. A., Jones, W. B., Davis, H., & Wein, D. (1991). Geochemical and petrological data for basalts from sites 756, 757 and 758: Implications for the origin and evolution of Ninetyeast Ridge. *Proceedings of the Ocean Drilling Program Scientific Results, 121,* 611-659. doi:10.2973/odp.proc.sr.121.163.1991

Frey, F. A., Pringle, M., Meleney, P., Huang, S., & Piotrowski, A. (2011). Diverse mantle sources for Ninetyeast Ridge magmatism: Geochemical constraints from basaltic glasses. *Earth and Planetary Science Letters, 303*(3-4), 215-224. doi:10.1016/j.epsl.2010.12.051

Frey, F. A., Silva, I. G. N., Huang, S., Pringle, M. S., Meleney, P. R. & Weis, D. (2015). Depleted components in the source of hotspot magmas: Evidence from the Ninetyeast Ridge (Kerguelen). *Earth and Planetary Science Letters, 426*, 293-304. doi:10.1016/j.epsl.2015.06.005

Gahalaut, V. K., Subrahmanyam, C., Kundu, B., Catherine, J. K., & Ambikapathy, A. (2010). Slow rupture in Andaman during 2004 Sumatra-Andaman earthquake: A probable consequence of subduction of 90°E ridge. *Geophysical Journal International, 180*(3), 1181-1186. doi:10.1111/j.1365-246X.2009.04449.x

Gauger, S., Kuhn, G., Gohl, K., Feigl, T., Lemenkova, P., & Hillenbrand, C. (2007). Swath-bathymetric mapping. *Reports on Polar and Marine Research, 557*, 38-45. doi:10.6084/m9.figshare.7439231

GEBCO Compilation Group. (2020). *GEBCO 2020 Grid*. doi:10.5285/a29c5465-b138-234d-e053-6c86abc040b9

GDAL/OGR Contributors. (2020). *GDAL/OGR geospatial data abstraction software library*. Open Source Geospatial Foundation. Retrieved from https://gdal.org

Gille, S. T., Yale, M. M., & Sandwell, D. T. (2000). Global correlation of mesoscale ocean variability with seafloor roughness from satellite altimetry. *Geophysical Research Letters, 27*(9), 1251-1254. doi:10.1029/1999GL007003

Gohl, K., Eagles, G., Udintsev, G., Larter, R. D., Uenzelmann-Neben, G., Schenke, H. W., Lemenkova, P., Grobys, J., Parsiegla, N., Schlueter, P., Deen, T., Kuhn, G., & Hillenbrand, C. D. (2006a). *Tectonic and sedimentary processes of the West Antarctic margin of the Amundsen Sea embayment and Pine Island Bay*. In Proceedings of the 2nd SCAR Open Science Meeting. Hobart, Australia. doi:10.6084/m9.figshare.7435484

Gohl, K., Uenzelmann-Neben, G., Eagles, G., Fahl, A., Feigl, T., Grobys, J., Just, J., Leinweber, V., Lensch, N., Mayr, C., Parsiegla, N., Rackebrandt, N., Schlüter, P., Suckro, S., Zimmermann, K., Gauger, S., Bohlmann, H., Netzeband, G., & Lemenkova, P. (2006b). *Crustal and sedimentary structures and geodynamic evolution of the West Antarctic Continental Margin and Pine Island Bay (pp. 11-12)*. Expeditionsprogramm Nr. 75 ANT XXIII/4 ANT XXIII/5,

Alfred Wegener Institute Helmholtz Centre for Polar and Marine Research. doi:10.13140/RG.2.2.16473.36961

Grevemeyer, I., & Flueh, E. R. (2000). Crustal underplating and its implications for subsidence and state of isostasy along the Ninetyeast Ridge hotspot trail. *Geophysical Journal International, 142*(2), 643-649. doi:10.1046/j.1365-246x.2000.00154.x

Grevemeyer, I., Flueh, E.R., Reichert, C., Bialas, J., Klaschen, D. & Kopp, C. (2001). Crustal architecture and deep structure of the Ninetyeast Ridge hotspot trail from active-source ocean bottom seismology. *Geophysical Journal International, 144*, 414-431. doi:10.1046/j.0956-540X.2000.01334.x

Gupta, R. P., & Sen, A. K. (1988). Imprints of the Ninety-East Ridge in the Shillong Plateau, Indian Shield. *Tectonophysics, 154*(3-4), 335-341. doi:10.1016/0040-1951(88)90111-4

Hédervari, P. (1982). A possible submarine volcano near the central part of Ninety-East Ridge, Indian ocean. *Journal of Volcanology and Geothermal Research, 13*(3-4), 199-211. doi:10.1016/0377-0273(82)90050-6

Hekinian, R. (1974). Petrology of the Ninety East Ridge (Indian Ocean) compared to other aseismic ridges. *Contributions to Mineralogy and Petrology, 43*, 125-147. doi:10.1007/BF00572715

Howland, M., Liss, B., Levy, T., & Najjar, M. (2020). Integrating digital datasets into public engagement through ArcGIS StoryMaps. *Advances in Archaeological Practice, 8*(4), 351-360. doi:10.1017/aap.2020.14

IHO-IOC GEBCO. (2020). *International hydrographic organization intergovernmental oceanographic commission general Bathymetric chart of the Ocean Gazetteer of Undersea Feature Names*. Retrieved from http://www.gebco.net/data_and_products/undersea_ feature_names

Klaučo, M., Gregorová, B., Stankov, U., Marković V., & Lemenkova, P. (2013). Determination of ecological significance based on geostatistical assessment: A case study from the Slovak Natura 2000 protected area. *Open Geosciences, 5*(1), 28-42. doi:10.2478/s13533-012-0120-0

Klaučo, M., Gregorová, B., Stankov, U., Marković, V., & Lemenkova, P. (2014). *Landscape metrics as indicator for ecological significance: Assessment of Sitno Natura 2000 sites, Slovakia (pp. 85-90)*. In Proceedings of the Ecology and Environmental Protection. Minsk, Belarus. doi:10.6084/m9.figshare.7434200

Klaučo, M., Gregorová, B., Koleda, P., Stankov, U., Marković, V., & Lemenkova, P. (2017). Land planning as a support for sustainable development based on tourism: A case study of Slovak Rural Region. *Environmental Engineering and Management Journal, 2*(16), 449-458. doi:10.30638/eemj.2017.045

Knudsen P., Andersen, O. B., & Tscheming, C. C. (1992). Altimetric gravity anomalies in the Norwegian-Greenland Sea: Preliminary results from the ERS-135 days repeat mission. *Geophysical Research Letters, 19*(17), 1795-1798. doi:10.1029/92GL01698

Krishna, K. S., Neprochnov, Y. P., Rao, D. G., & Grinko, B. N. (2001). Crustal structure and tectonics of the Ninetyeast Ridge from seismic and gravity studies. *Tectonics, 20*(3), 416-433. doi:10.1029/2001TC900004

Krishna, K. S. (2003). Structure and evolution of the Afanasy Nikitin seamount, buried hills and 85°E Ridge in the northeastern Indian Ocean. *Earth and Planetary Science Letters, 209*, 379-394. doi:10.1016/S0012-821X(03)00081-5

Krishna, K. S., Bull, J. M., Ishizuka, O., Scrutton, R. A., Jaishankar, S., & Banakar, V. K. (2014). Growth of the Afanasy Nikitin seamount and its relationship with the 85°E Ridge, northeastern Indian Ocean. *Journal of Earth System Science, 123*, 33-47. doi:10.1007/s12040-013-0392-x

Kumar, P., Yuan, X., Kumar, M. R., Kind, R., Li, X., & Chadha, R. K. (2007). The rapid drift of the Indian tectonic plate. *Nature, 449*, 894-897. doi:10.1038/nature06214

Lemenkova, P. (2020a). Variations in the bathymetry and bottom morphology of the Izu-Bonin Trench modelled by GMT. *Bulletin of Geography: Physical Geography Series, 18*(1), 41-60. doi:10.2478/bgeo-2020-0004

Lemenkova, P. (2020b). Applying automatic mapping processing by GMT to bathymetric and geophysical data: Cascadia subduction zone, Pacific Ocean. *Journal of Environmental Geography, 13*(3-4), 15-26. doi:10.2478/jengeo-2020-0008

Lemenkova, P. (2020c). Sediment thickness in the Bay of Bengal and Andaman Sea compared with topography and geophysical settings by GMT. *Ovidius University Annals Series: Civil Engineering, 22*, 13-22. doi:10.2478/ouacsce-2020-0002

Lemenkova, P. (2020d). Insights on the Indian Ocean tectonics and geophysics supported by GMT. *Risks and Catastrophes Journal, 27*(2), 67-83. doi:10.24193/RCJ2020_12

Lemenkova, P. (2020e). GEBCO gridded bathymetric datasets for mapping Japan trench geomorphology by means of GMT scripting toolset. *Geodesy and Cartography, 46*(3), 98-112. doi:10.3846/gac.2020.11524

Lemenkova, P. (2020f). GEBCO and ETOPO1 gridded datasets for GMT based cartographic mapping of Hikurangi, Puysegur and Hjort Trenches, New Zealand. *Acta Universitatis Lodziensis. Folia Geographica Physica, 19*, 7-18. doi:10.18778/1427-9711.19.01

Lemenkova, P. (2019a). Geomorphological modelling and mapping of the Peru-Chile Trench by GMT. *Polish Cartographical Review, 51*(4), 181-194. doi:10.2478/pcr-2019-0015

Lemenkova, P. (2019b). Topographic surface modelling using raster grid datasets by GMT: example of the Kuril-Kamchatka Trench, Pacific Ocean. *Reports on Geodesy and Geoinformatics, 108*(1), 9-22. doi:10.2478/rgg-2019-0008

Lemenkova, P. (2019c). GMT based comparative analysis and geomorphological mapping of the Kermadec and Tonga Trenches, Southwest Pacific Ocean. *Geographia Technica, 14*(2), 39-48. doi:10.21163/GT_2019.142.04

Lemenkova, P. (2019d). Geophysical modelling of the middle America Trench using GMT. *Annals of Valahia University of Targoviste Geographical Series, 19*(2), 73-94. doi:10.6084/m9.figshare.12005148

Lemenkova, P. (2019e). Automatic data processing for Visualising Yap and Palau Trenches by Generic mapping tools. *Cartographic Letters, 27*(2), 72-89. doi:10.6084/m9.figshare.11544048

Lemenkova, P. (2019f). Statistical analysis of the Mariana Trench Geomorphology using R Programming language. *Geodesy and Cartography, 45*(2), 57-84. doi:10.3846/gac.2019.3785

Lemenkova, P. (2019g). Calculating slope gradient variations in the submarine landforms by R and Python statistical libraries. *MANAS Journal of Engineering, 7*(2), 99-113. doi:10.6084/m9.figshare.11454768

Lemenkova, P. (2019h). AWK and GNU Octave programming languages integrated with Generic Mapping tools for geomorphological analysis. *GeoScience Engineering, 65*(4), 1-22. doi:10.35180/gse-2019-0020

Lemenkova, P. (2018). R scripting libraries for comparative analysis of the correlation methods to identify factors affecting Mariana Trench formation. *Journal of Marine Technology and Environment, 2*, 35-42. doi:10.6084/m9.figshare.7434167

Lemoine, F. G., Kenyon, S. C., Factor, J. K., Trimmer, R. G., Pavlis, N. K., Chinn, D. S., Cox, C. M., Klosko, S. M., Luthcke, S. B., Torrence, M. H., Wang, Y. M., Williamson, R. G., Pavlis, E. C., Rapp, R. H., & Olson, T. R. (1998). *The development of the joint NASA GSFC and the National Imagery and Mapping Agency (NIMA) geopotential model EGM96.* NASA/TP-1998-206861.

Liu, C., Sandwell, D. T., & Curray, J. R. (1982). The negative gravity field over the 85° E ridge. *Journal of Geophysical Research, 87*, 7673-7686. doi:10.1029/JB087iB09p07673

Liu, C.S., Curray, J.R., & McDonald, J.M. (1983). New constraints on the tectonic evolution of eastern Indian Ocean. *Earth and Planetary Science Letters, 65*, 331-342. doi:10.1016/0012-821X(83)90171-1

Marks, K. M., Smith, W. H. F. & Sandwell, D. T. (2010). Evolution of errors in the altimetric bathymetry model used by Google Earth and GEBCO. *Marine Geophysical Researches, 31*, 223-238. doi:10.1007/s11001-010-9102-0

McKenzie, D. P., & Bowin, C. (1976). The relationship between bathymetry and gravity in the Atlantic Ocean. *Journal of Geophysical Research, 81*, 1903-1915. doi:10.1111/j.1365-246X.1985.tb05166.x

Mukhopadhyay, M., & Krishna, M. B. R. (1995). Gravity anomalies and deep structure of the Ninetyeast Ridge north of the equator, eastern Indian Ocean: A hot spot trace model. *Marine Geophysical Research, 17*, 201-216. doi:10.1007/BF01203426

Neal, C. R., Sager, W. W., Sano, T., & Erba, E. (2015). *The origin, evolution, and environmental impact of Oceanic Large Igneous provinces*. Geological Society of America. doi:10.1130/SPE511

Nobre, I. G. S., Weis, D., Scoates, J. S., & Barling, J. (2013). The Ninetyeast ridge and its relation to the Kerguelen, Amsterdam and St. Paul Hotspots in the Indian Ocean. *Journal of Petrology, 54*(6), 1177-1210. doi:10.1093/petrology/egt009

Pavlis, N. K., Holmes, S. A., Kenyon, S. C., & Factor, J. K. (2012). The development and evaluation of the Earth Gravitational Model 2008 (EGM2008). *Journal of Geophysical Research, 117*, B04406. doi:10.1029/2011JB008916

Peirce, J. W. (1978). The northward motion of India since the Late Cretaceous. *Geophysical Journal International*, *52*(2), 277-311. doi:10.1111/j.1365-246X.1978.tb04234.x

Petroy, D. E., & Wiens, D. A. (1989). Historical seismicity and implications for diffuse plate convergence in the northeast Indian Ocean. *Journal of Geophysical Research, 94*, 12301-12319. doi:10.1029/JB094iB09p12301

Rao, D. G., Krishna, K. S., & Sar, D. (1997). Crustal evolution and sedimentation history of the Bay of Bengal since the Cretaceous. *Journal of Geophysical Research, 102*(B8), 17747-17768. doi:10.1029/96JB01339

Ratheesh, R. T. K., & Windley, B. F. (2013). Spatial variations of effective elastic thickness over the Ninetyeast Ridge and implications for its structure and tectonic evolution. *Tectonophysics, 608*, 847-856. doi:10.1016/j.tecto.2013.07.034

Rajesh, S., & Majumdar, T. J. (2009). Geoid height versus topography of the Northern Ninetyeast Ridge: Implications on crustal compensation. *Marine Geophysical Research 30*, 251-264. doi:10.1007/s11001-010-9088-7

Royer, J. Y., & Sandwell, D. T. (1989). Evolution of the eastern Indian Ocean since the Late Cretaceous: Constraints from Geosat altimetry, *Journal of Geophysical Research*, *94*(B10), 13755-13782. doi:10.1029/JB094iB10p13755

Royer, J. Y., Sclater, J. G. & Sandwell, D. T. (1989). A preliminary tectonic fabric chart of the Indian Ocean. *Proceedings of the Indian Academy of Sciences: Earth & Planetary Sciences, 98*, 7-24. doi:10.1007/BF02880373

Royer, J. Y., Peirce, J. W., & Weissel, J. K. (1991). Tectonic constraints on the hot-spot formation of Ninetyeast Ridge. *Proceedings of the Ocean Drilling Program: Scientific Results, 121*, 763-775. doi:10.2973/odp.proc.sr.121.122.1991

Royer, J. Y., Sclater, J. G., Sandwell, D. T., Cande, S. C., Schlich, R., Munschy, M., Dyment, J., Fisher, R. L., Müller, R. D., Coffin, M. F., Patriat, P., & Bergh, H. W. (1992). *Appendix 1: Indian Ocean plate reconstructions since the Late Jurassic*. In Duncan, R. A., Rea, D. K., Kidd, R. B., Rad, U. V., & Weissel, J. K. (Eds.). Synthesis of Results from Scientific Drilling in the Indian Ocean. doi:10.1029/GM070p0471

Sager, W. W., Bull, J. M., & Krishna, K. S. (2013). Active faulting on the Ninetyeast Ridge and its relation to deformation of the Indo-Australian plate. *Journal of Geophysical Research, 118*, 4648-4668. doi:10.1002/jgrb.50319

Sandwell, D. T., & Liu, C. S. (1985). *The gravity field of topography buried by sediments. Conference Paper, NTRS*. NASA, Washington Geopotential Res. Mission (GRM). Document ID: 19860003396.

Sandwell D. T. (1992). Antarctic marine gravity field from high-density satellite altimetry. *Geophysical Journal International, 109,* 437-448. doi:10.1111/j.1365-246X.1992.tb00106.x

Sandwell, D. T., & McKenzie, K. R. (1989). Geoid height versus topography for oceanic plateaus and swells. *Journal of Geophysical Research, 94*(B6), 7403-7418. doi:10.1029/JB094iB06p07403

Sandwell, D., Garcia, E., Soofi, K., Wessel, P., Chandler, M., & Smith, W. H. F. (2013). Toward 1-mGal accuracy in global marine gravity from CryoSat-2, Envisat, and Jason-1. *The Leading Edge, 32*(8), 892. doi:10.1190/tle32080892.1

Sandwell, D. T., Müller, R. D., Smith, W. H. F., Garcia, E., & Francis, R. (2014). New global marine gravity model from CryoSat-2 and Jason-1 reveals buried tectonic structure. *Science, 346*(6205), 65-67. doi:10.1126/science.1258213

Sansò F., Reguzzoni M., & Barzaghi R. (2019). *The earth gravity field: Basics.* Geodetic Heights. Springer Geophysics. Springer. doi:10.1007/978-3-030-10454-2_3

Schenke, H. W., & Lemenkova, P. (2008). Zur Frage der Meeresboden-Kartographie: Die Nutzung von AutoTrace Digitizer für die Vektorisierung der Bathymetrischen Daten in der Petschora-See. *Hydrographische Nachrichten, 81*, 16-21. doi:10.6084/m9.figshare.7435538

Schenke, H. (2016). *General Bathymetric Chart of the Oceans (GEBCO).* In Harff, J., Meschede, M., Petersen, S., & Thiede, J. (Eds.). Encyclopedia of Marine Geosciences. Encyclopedia of Earth Sciences Series. Springer. doi:10.1007/978-94-007-6238-1_63

Sclater, J. G., & Fisher, R. L. (1974). Evolution of the east central Indian ocean, with emphasis on the tectonic setting of the Ninetyeast Ridge. *Geological Society of America Bulletin, 85*(5), 683-702. doi:10.1130/0016-7606(1974)85<683:EOTECI>2.0.CO;2

Shang, L., Hu, G., Yuan, Z., Qi, J., & Pan, J. (2020). Tectonic structure and origin of the 85°E ridge, Northeastern Indian Ocean: A review and new observations. *Marine Geology & Quaternary Geology, 40*(4), 1-16. doi:10.16562/j.cnki.0256-1492.2020042201

Silva, I. G. N., Weis, D., Scoates, J. S. & Barling, J. (2013). The Ninetyeast ridge and its relation to the Kerguelen, Amsterdam and St. Paul Hotspots in the Indian Ocean. *Journal of Petrology, 54*(6), 1177-1210. doi:10.1093/petrology/egt009

Smith, G. M., Gee, J., & Klootwijk, C. T. (1991). Magnetic petrology of basalts from Ninetyeast ridge. *Proceedings of the Ocean Drilling Program, Scientific Results, 121*, 525-545. doi:10.2973/odp.proc.sr.121.154.1991

Smith, W. H. F. (1993). On the accuracy of digital bathymetric data. *Journal of Geophysical Research, 98*(B6), 9591-9603. doi:10.1029/93JB00716

Smith, W. H. F., & Sandwell, D. T. (1997). Global seafloor topography from Satellite altimetry and ship depth soundings. *Science, 277*, 1956-1962. doi:10.1126/science.277.5334.1956

Smith, P. (1978). How Ninetyeast Ridge formed. *Nature, 272*, 752-753. doi:10.1038/272752a0

Small, C., Cochran, J. R., Sempéré, J. C., & Christie, D. (1999). The structure and segmentation of the Southeast Indian Ridge. *Marine Geology*, *161*(1), 1-12. doi:10.1016/S0025-3227(99)00051-1

Souriau, A. (1981). The upper mantle beneath Ninetyeast Ridge and Broken Ridge, Indian Ocean, from surface waves. *Geophysical Journal International, 67(*2), 359-374. doi:10.1111/j.1365-246X.1981.tb02755.x

Sreejith, K. M., Unnikrishnan, P., & Radhakrishna, M. (2019). Isostasy and crustal structure of the Chagos-Laccadive Ridge, Western Indian Ocean: Geodynamic implications. *Journal of Earth System Science, 128*, 157. doi:10.1007/s12040-019-1161-2

Stein, S., & Okal, E. O. (1978). Seismicity and tectonics of the Ninetyeast Ridge area: Evidence for internal deformation of the Indian plate. *Journal of Geophysical Research, 83*, 2233-2246. doi:10.1029/JB083iB05p02233

Steinberger, B. (2016). Topography caused by mantle density variations: Observation-based estimates and models derived from tomography and lithosphere thickness. *Geophysical Journal International, 205*(1), 604-621. doi:10.1093/gji/ggw040

Stevens, D. E., McNeill, L. C., Henstock, T. J., Delescluse, M., Chamot-Rooke, N., & Bull, J. M. (2020). A complete structural model and kinematic history for distributed deformation in the Wharton Basin. *Earth and Planetary Science Letters, 538,* 116218. doi:10.1016/j.epsl.2020.116218

Stocks, T. (1960). Zur Bodengestalt des Indischen Ozeans. Bericht über den gegenwärtigen Stand der Forschung. *Erdkunde, 14*(3), doi:10.3112/erdkunde.1960.03.01

Subrahmanyam, C., Gireesh, R., Chand, S., Kamesh Raju, K. A., & Gopal, D. R. (2008). Geophysical characteristics of the Ninetyeast Ridge: Andaman island arc/trench convergent zone. *Earth and Planetary Science Letters, 266,* 29-45. doi:10.1016/j.epsl.2007.10.016

Suetova, I. A., Ushakova, L. A., & Lemenkova, P. (2005a). Geoinformation mapping of the Barents and Pechora Seas. *Geography and Natural Resources, 4*, 138-142. doi:10.6084/m9.figshare.7435535

Suetova, I., Ushakova, L., & Lemenkova, P. (2005b). *Geoecological mapping of the Barents Sea using GIS*. In Proceedings of the International Cartographic Conference. La Coruna, Spain. doi:10.6084/m9.figshare.7435529

Tiwari, V. M., Diament, M., & Singh, S. C. (2003). Analysis of satellite gravity and bathymetry data over Ninety-East Ridge: Variation in the compensation mechanism and implication for emplacement process. *Journal of Geophysical Research, 108*(B2), 2109. doi:10.1029/2000JB000047

Tozer, B, Sandwell, D. T., Smith, W. H. F., Olson, C., Beale, J. R., & Wessel, P. (2019). Global bathymetry and topography at 15 arc sec: SRTM15+. *Earth and Space Science, 6*, 1847-1864. doi:10.1029/2019EA000658

Weis, D., White, W. M., Frey, F. A., Duncan, R. A., Fisk, M. R., Dehn, J., Ludden, J., Saunders, A., & Storey, M. (1993). The influence of mantle plumes in generation of Indian Oceanic Crust. *Geophysical Monograph Series, 70*, 57-89. doi:10.1029/GM070p0057

Weis, D., Frey, F. A., Saunders, A., & Gibson, I. (1991). Ninetyeast Ridge (Indian Ocean): A 5,000 km record of a duple mantle plume. *Geology, 19,* 99-102. doi:10.1130/0091-7613(1991)019<0099:NRIOAK>2.3.CO;2

Wessel, P., & Smith, W. H. F. (1991). Free software helps map and display data. *Eos Transactions of the American Geophysical Union, 72*(41), 441. doi:10.1029/90EO00319

Wessel, P., & Smith, W. H. F. (1996). A global self-consistent, hierarchical, high-resolution shoreline database. *Journal of Geophysical Research, 101*, 8741-8743. doi:10.1029/96JB00104

Wessel, P., & Smith, W. H. F. (1998). New version of the Generic Mapping Tools released. *Eos Transactions of the American Geophysical Union, 76*(33), 329. doi:10.1029/98EO00426

Wessel, P., Smith, W. H. F., Scharroo, R., Luis, J. F., & Wobbe, F. (2013). Generic mapping tools: Improved version released. *Eos Transactions American Geophysical Union, 94*(45), 409-410. doi:10.1002/2013EO450001

Wessel, P., Luis, J. F., Uieda, L., Scharroo, R., Wobbe, F., Smith, W. H. F., & Tian, D. (2019). The generic mapping tools version 6. *Geochemistry, Geophysics, Geosystems, 20*, 5556-5564. doi:10.1029/2019GC008515